Published on 03 November 2020. Downloaded by Changchun Institute of Optics, Fine Mechanics and Physics, CAS on 4/2/2021 4:48:27 AM.

Nanoscale

ROYAL SOCIETY OF CHEMISTRY

PAPER

View Article Online
View Journal | View Issue

Check for updates

Cite this: *Nanoscale*, 2020, **12**, 23732

Effects of dielectric screening on the excitonic and critical points properties of WS_2/MoS_2 heterostructures†

Xudan Zhu, [a] Junbo He,[a] Rongjun Zhang, *[a] Chunxiao Cong, *[b] Yuxiang Zheng,[a] Hao Zhang, [a] Shanwen Zhang*[c] and Liangyao Chen[a]

Received 17th June 2020,
Accepted 1st November 2020

DOI: 10.1039/d0nr04591h

rsc.li/nanoscale

Vertical van der Waals heterostructures have aroused great attention for their promising application in next-generation nanoelectronic and optoelectronic devices. The dielectric screening effect plays a key role in the properties of two-dimensional (2D) heterostructures. Here, we studied the dielectric screening effects on the excitonic properties and critical points (CPs) of the WS_2/MoS_2 heterostructure using spectroscopic ellipsometry (SE). Owing to the type-II band alignment of the WS_2/MoS_2 heterostructure, charged carriers spatially separated and created an interlayer exciton, and the transition energy and binding energy have been accurately found to be 1.58 ± 0.050 eV and 431.39 ± 127.818 meV by SE, respectively. We found that stacking the WS_2/MoS_2 vertical heterostructure increases the effective dielectric screening compared with the monolayer counterparts. The increased effective dielectric screening in the WS_2/MoS_2 heterostructure weakens the long-range Coulomb force between electrons and holes. Consequently, the quasi-particle band gap and the exciton binding energies are reduced, and because of the orbital overlap, more CPs are produced in the WS_2/MoS_2 heterostructure in the high photon energy range. Our results not only shed light on the interpretation of recent first-principles studies, but also provide important physical support for improving the performance of heterostructure-based optoelectronic devices with tunable functionalities.

1. Introduction

Recently, inspired by the discovery of graphene, more two-dimensional (2D) materials, such as black phosphorus, hexagonal boron nitride, and transition metal dichalcogenides (TMDs), have been explored.[1–4] Different from bulk materials, 2D materials have exotic properties due to their reduced dimensions and quantum confinement effects.[5–7]

Moreover, the weak van der Waals (vdW) bonding between the layers and the dangling-bond-free surface of the 2D layered materials make it possible to construct arbitrary vertical vdW heterostructures without the restriction of lattice matching.[1,5,8,9] The stacked heterostructures can not only preserve the inherently unique physical properties of the individual layers but also create new properties through interlayer charge transfer,[2,10–12] interlayer coupling (interlayer distance),[6,9,10] dielectric screening,[8,11–13] and crystal orientation.[6,7] Among the various vertical vdW heterostructures, MoS_2/WS_2 heterostructures have attracted widespread attention in the field of optoelectronics, especially in light detection and light-harvesting devices.[7,14] This is due to their type-II (staggered gap) band alignment revealed by recent first-principles studies.[15] Type-II band alignment promotes the charge transfer and separation at the interface,[6,16,17] which significantly enhances the efficiency of sunlight capture.[18]

It is known that environmental dielectric screening plays a crucial role in tuning the electronic band structure and exciton binding energy of monolayer (1L) 2D materials,[12,13] and the

[a]*Key Laboratory of Micro and Nano Photonic Structures, Ministry of Education, Shanghai Engineering Research Center of Ultra-Precision Optical Manufacturing, School of Information Science and Engineering, Fudan University, Shanghai 200433, China. E-mail: rjzhang@fudan.edu.cn*

[b]*State Key Laboratory of ASIC and System, School of Information Science and Engineering, Fudan University, Shanghai 200433, China. E-mail: cxcong@fudan.edu.cn*

[c]*Grating Technology Laboratory, Changchun Institute of Optics and Fine Mechanics and Physics, Chinese Academy of Sciences, Changchun, Jilin 130033, China. E-mail: zhshwen007@163.com*

† Electronic supplementary information (ESI) available: AFM images of 1L-MoS_2, 1L-WS_2, and WS_2/MoS_2 heterostructure samples; PL spectra of sapphire substrate, which we used in all three samples; PL spectra analysis of 1L-MoS_2, 1L-WS_2, and WS_2/MoS_2 heterostructure samples; detailed information of the point-by-point method used to fit the ellipsometric parameters, including the optical model and the specific self-check procedure; SCP model fitting CP properties of the films, at the same time, all the fitting parameters of CPs are listed in Table S1; excitonic properties fitting parameters are shown in Table S2. See DOI: 10.1039/d0nr04591h

This journal is © The Royal Society of Chemistry 2020

Published on 03 November 2020. Downloaded by Changchun Institute of Optics, Fine Mechanics and Physics, CAS on 4/2/2021 4:48:27 AM.

exciton binding energy connects the optical transition energy to the quasi-particle band gap.[4] By modifying the long-range Coulomb interaction between electrons and holes, the band gap and exciton binding energy can be tailored on the order of several hundred meV.[19] Turning this argument around, one can engineer the exciton binding energy and critical point (CP) properties by tailoring environmental dielectric screening through the formation of hybrid structures,[8,13] using different substrates[4,12] or implementing a gate field.[9] For many of these intriguing new observations, a thorough understanding of how dielectric screening affects the optical properties of 2D materials is fundamentally important for further modulating excitonic properties. Nonetheless, studies on environmental dielectric screening are still at the theoretical stage, and experimental demonstrations are still lacking, which gives us motivation to systematically explore the role of dielectric screening in vertical heterostructures.

In this work, we revealed the broadband CPs and excitonic properties of the WS_2/MoS_2 heterostructure by spectroscopic ellipsometry (SE), which is a submonolayer-sensitive and non-destructive technique for investigating the optical properties of 2D materials and their heterostructures.[3,20–22] Here, eight CPs (named in order of transition energies: A_M–H_M) of 1L-MoS_2, nine CPs (named in order of transition energies: A_W–I_W) of 1L-WS_2, and ten CPs of the WS_2/MoS_2 heterostructure (named in order of transition energies: A_H–J_H) were obtained, the transition energies of which are in accordance with the transitions in electronic band structures predicted by previous theoretical studies. The *Van Hove singularities* of these CPs were discussed in detail. Moreover, the spin–orbit splitting energies of 1L-TMD films were obtained and the binding energies of the excitons in 1L-WS_2, 1L-MoS_2, and the WS_2/MoS_2 heterostructure were obtained. The discrete states of the exciton observed in 1L-TMD thin films and their heterostructure were modeled using a broadened Lorentzian line shape, from which we obtained the binding energies of the excitons in 1L-WS_2, 1L-MoS_2, and the WS_2/MoS_2 heterostructure. Our results not only provide experimental support for theoretical calculations, but also provide guidance for engineering the excitonic properties and electronic band structures of 2D materials by constructing vertical vdW heterostructures, which is crucial to the potential optoelectronic applications based on vertical vdW heterostructures.

2. Experimental section

2.1. Synthesis of monolayer and heterostructure samples

Large-area 1L-WS_2 and 1L-MoS_2 samples (1×1 cm^2) were grown on SiO_2/Si substrates separately by the chemical vapor deposition (CVD) method and then transferred onto sapphire substrates.[23,24] By using sapphire substrates, the back-reflection of light in the SiO_2 vanishes, thus improving the accuracy of SE fitting.[25] The 1L samples were annealed at 350 °C for 2 h in a vacuum. Then, the MoS_2 film was transferred onto the WS_2 film, followed by the same annealing procedure. The annealing process is necessary for forming a clean interface between MoS_2 and WS_2, which is required for efficient charge transfer and excellent excitonic behaviour.[26]

2.2. Morphological characterization

Atomic force microscopy (AFM, AIST-NT System) was carried out in the contact mode, with the aim of evaluating the surface roughness of the individual transferred samples of 1L-WS_2, 1L-MoS_2, and the WS_2/MoS_2 heterostructure on sapphire substrates.

2.3. Optical spectroscopic examination

Raman and photoluminescence (PL, SPEX/403) spectra were measured at room temperature and excitation wavelength of 532 nm. The transmission spectra of our samples were obtained using a spectrophotometer (Jinghua UV1901) with the wavelength in the range of 360 to 1100 nm. The optical properties of the three samples were explored by SE (J. A. Woollam, Inc. M2000X-FB-300XTF) at room temperature. Ellipsometric data (ψ, Δ) were collected over a photon energy range from 1.2 to 6.5 eV (513 data points) at a fixed incident angle of 65 degrees.

3. Results and discussion

3.1. Basic characterization

Fig. 1a shows a schematic illustration of the WS_2/MoS_2 heterostructure. With reference to the reported theoretically calculated conduction band minimum (CBM) and valence band maximum (VBM) levels of 1L-MoS_2 and 1L-WS_2,[27] the band alignment of the WS_2/MoS_2 heterostructure is shown in Fig. 1b. This shows that the WS_2/MoS_2 heterostructure is of type-II band alignment, in which electrons and holes are inclined to transfer across the interface between the two 1L-TMDs layers. The Raman spectra of 1L-WS_2, 1L-MoS_2, and the WS_2/MoS_2 heterostructure are presented in Fig. 1c, which also shows the decisive monolayer structures of the MoS_2 and WS_2 films.[28,29] Meanwhile, the in-plane mode $E_{2g}{}^1$ and out-plane mode A_{1g} of the heterostructure film slightly redshifts, compared with the corresponding 1L-TMD films, due to the charge transfer and strain in the interface between the two 1L-TMDs.[1,30] The AFM images shown in ESI (Fig. S1a–c†) demonstrate that there are no discernible contamination of the surface of 1L-WS_2, 1L-MoS_2, and WS_2/MoS_2 heterostructure films transferred on sapphire substrates.

PL spectra of 1L-WS_2, 1L-MoS_2, and the WS_2/MoS_2 heterostructure are shown in ESI as Fig. S3.† The energies of neutral A excitons (X_A) of 1L-MoS_2 and 1L-WS_2 are 1.85 eV and 2.00 eV, respectively. Charged excitons (trions) have also been observed in the PL spectra of 1L-WS_2, 1L-MoS_2, and the WS_2/MoS_2 heterostructure. We decomposed the PL spectra of WS_2/MoS_2 heterostructure into four major components by Gaussian fitting, which are interlayer exciton (1.60 eV), 1L-MoS_2 intralayer trion (1.79 eV), 1L-MoS_2 intralayer A exciton (1.87 eV), and 1L-WS_2 intralayer A exciton (2.00 eV), respectively. The

Published on 03 November 2020. Downloaded by Changchun Institute of Optics, Fine Mechanics and Physics, CAS on 4/2/2021 4:48:27 AM.

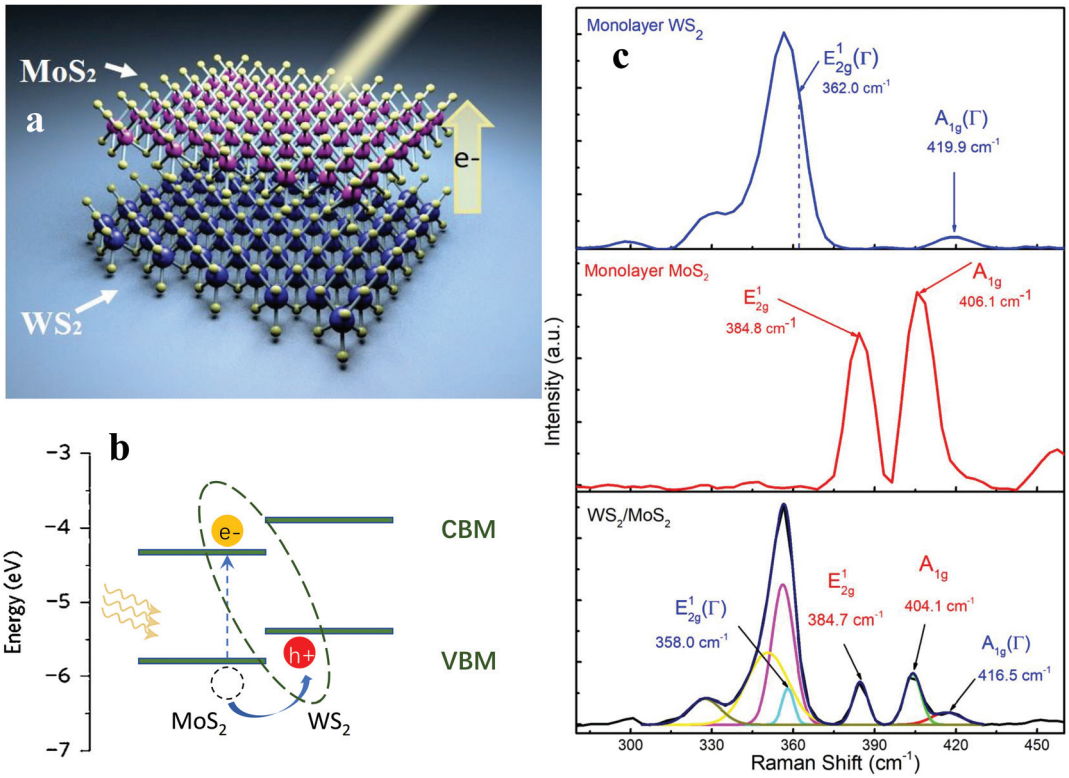

Fig. 1 (a) Schematic illustration of the WS_2/MoS_2 heterostructure film. (b) Illustration of type-II band alignment of the WS_2/MoS_2 heterostructure. (c) Raman spectra of monolayer MoS_2 and WS_2 and WS_2/MoS_2 heterostructure samples with the wavenumber varying from 280 to 460 cm^{-1}, where only the typical peaks of these three types of samples were displayed for comparison. The Raman results were obtained under 532 nm laser excitation at room temperature, and the detailed multiple peaks were obtained by Lorentz fitting.

interlayer exciton stems from the band alignment of the WS_2/MoS_2 heterostructure as shown in Fig. 1b. Detailed information is supplied in the ESI.†

3.2. Dielectric functions and optical conductivities

The complex dielectric functions ($\varepsilon(E)$) of the 1L-WS_2, 1L-MoS_2, and WS_2/MoS_2 heterostructure films were derived by fitting the ellipsometric (ψ, Δ) spectra using the point-by-point method.[31] A vertical stacking optical model consisting of sapphire substrate/thin film sample/air ambient was used in the fitting procedure. The detailed fitting process and self-check demonstration are presented in the ESI (section 3).† Fig. 2a shows the complex dielectric functions of the samples, from which the real part of the complex film conductivity (in units of $G_0 = 2e^2/h$) of all samples was derived (shown in Fig. 2b). The detailed calculation equations are introduced in the ESI (section 3.2).† The optical properties of thin films can be expressed through the real part of the complex film conductivity. Neglecting the excitonic effect, the optical conductivity of 1L-TMDs can be described by a *step function*:[32]

$$\Theta(\hbar\omega - E_g), \tag{1}$$

indicating they are indeed direct bandgap semiconductors. The WS_2/MoS_2 heterostructure is an indirect semiconductor, which is also confirmed by the absorption coefficient spectra or absorbance spectra (shown in ESI as Fig. S6b†). As shown in a previous theoretical study, the CBM of the WS_2/MoS_2 heterostructure locates at the K point in the BZ, but the VBM locates at the Γ point in the BZ.[17] Furthermore, the intrinsic optical conductivity relates to the mobility and lifetime of carriers as well as the temperature:

$$\sigma = \sigma_n + \sigma_p = nq\mu_n + pq\mu_p = \frac{nq^2\tau_n}{m_n^*} + \frac{pq^2\tau_p}{m_p^*}, \tag{2}$$

where n, σ_n, τ_n, and m_n^* denote the concentration, optical conductivity, lifetime, and effective mass of electrons in thin films, respectively; and p, σ_p, τ_p, and m_p^* denote those of holes. In addition, photoexcitation can produce an additional optical conductivity *via* optical injection of charged carriers, which can be calculated from eqn (3):

$$\Delta\sigma = \Delta nq\mu_n + \Delta pq\mu_p = \Delta nq(\mu_n + \mu_p), \tag{3}$$

where $\Delta\sigma$ is the additional optical conductivity; Δn and Δp are the concentrations of the optical injected charged carriers (for electrons and holes: $\Delta n = \Delta p$); and μ_n and μ_p denote the mobility of electrons and holes, respectively. According to a previous study,[26] the exciton diffusion coefficients of carriers in the heterostructure are similar to that of the carriers in individual 1L-TMDs. That is to say, the spatial indirect nature of the charge-transfer excitons in WS_2/MoS_2 heterostructures does

 This journal is © The Royal Society of Chemistry 2020

Published on 03 November 2020. Downloaded by Changchun Institute of Optics, Fine Mechanics and Physics, CAS on 4/2/2021 4:48:27 AM.

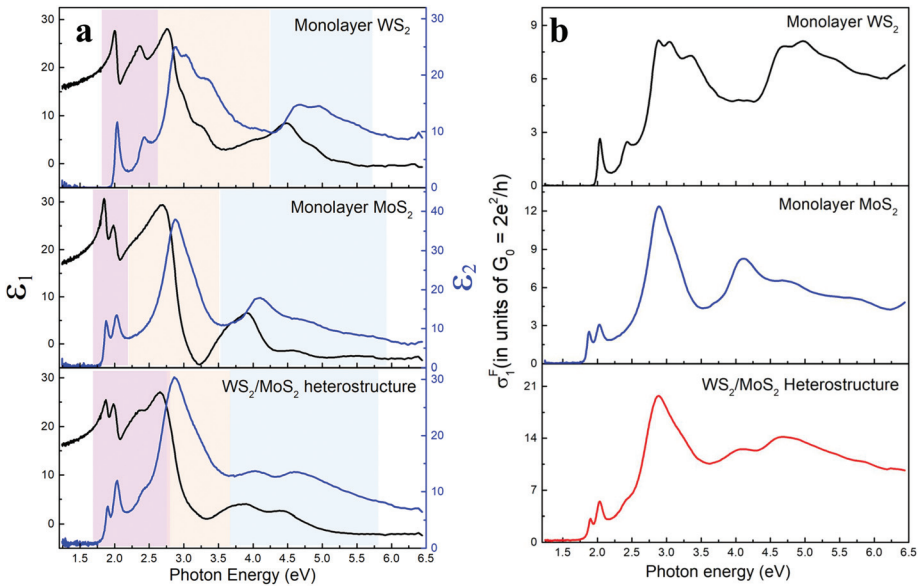

Fig. 2 (a) Complex dielectric functions ($\varepsilon(E)$); and (b) the real part of the complex film conductivity ($\sigma_1^F(E)$, in units of $G_0 = 2e^2/h$) of the 1L-MoS_2, 1L-WS_2 and WS_2/MoS_2 heterostructure samples. The purple, orange, and blue areas represent the M_0, M_1, and non-defined types of *Van Hove singularities*, respectively.

not significantly change its in-plane mobility. Thus, the WS_2/MoS_2 heterostructure film shows the largest optical conductivity compared to that of 1L-TMDs, indicating its largest photoexcitation charged carrier concentration, according to eqn (3). Although the photoexcitation electrons transfer across layers forming interlayer excitons, leading to the PL quenching feature (shown as Fig. S3†), the electrostatic Coulomb force binds the electrons and holes together to form charged transfer excitons (interlayer and intralayer excitons). These charged transfer excitons will still contribute to the total optical conductivity. Our findings can be extended to other heterostructures with type-II band alignment, which will provide guidance for optoelectronic and electronic devices based on heterostructures.

3.3. Critical points and corresponding Van Hove singularities

The series of sharp peaks in the dielectric function spectra are assigned to CPs. It is not accurate to extract the transition energies of CPs by simply locating the energies at which the peaks occur.[21] Here, we numerically differentiate the dielectric functions. In the vicinity of a CP, the dielectric response can be represented by the standard critical point (SCP) model:[3,21,22]

$$\varepsilon(E) = C - Ae^{-i\varphi}(E - E_{\mathrm{th}} + i\Gamma)^n, \quad (4)$$

where C is the nonresonant part due to other CPs; A is the amplitude; φ is the phase angle representing the coupling between two CPs;[3] and E_{th} is the threshold energy (*i.e.* CP energy). As the CPs represent the interband transitions, the E_{th} is the corresponding interband energy difference where the transitions occur, and Γ is the phenomenological broadening parameter relating to scattering rates.[21] In particular, the exponent n takes the value of $-1/2$, 0 (logarithmic, *i.e.*, $\ln(E - E_{\mathrm{th}} + i\Gamma)$), and 1/2 for one-dimensional (1D), 2D, and three-dimensional (3D) CPs, respectively. In addition, in order to remove the background disturbance signal, the CP properties were obtained by fitting the second derivative of the complex dielectric functions (real and imaginary parts simultaneously) with respect to photon energy ($d^2\varepsilon/dE^2$). Here, we took $n = -1$. The equation is given as eqn (5):[3,21,22]

$$\frac{d^2\varepsilon}{dE^2} = \frac{2Ae^{i\varphi}}{(E - E_{\mathrm{th}} + i\Gamma)^3} \quad (5)$$

Fig. S7a in ESI† shows the $d^2\varepsilon/dE^2$ of the 1L-TMDs and the heterostructure, in which the CP energies are depicted as vertical dashed lines. Notably, before the fitting procedure, a smoothening process was implemented on the $d^2\varepsilon/dE^2$ spectra, using the Savitzky–Golay method.[33] Fig. S7b† depicts the experimental and best-match fitting curves for $d^2\varepsilon/dE^2$, which are in excellent agreement with each other as expected. We labelled the CP energies in order of increasing energy as A–J, and distinguished the CPs for three samples using different subscripts (subscripts M, W, and H represent the CPs of 1L-MoS_2, 1L-WS_2, and the WS_2/MoS_2 heterostructure, respectively). The extracted CP energies (E_{th}) of 1L-WS_2, 1L-MoS_2, and the WS_2/MoS_2 heterostructure derived from eqn (5) are summarized in Table 1 and plotted in Fig. 3a. Meanwhile, all the fitting parameters are provided in ESI as Table S1.† Notably, the effective vertical dielectric constants of 1L-WS_2, 1L-MoS_2 and the bilayer TMD heterostructure are 6.0, 6.3 and 6.5, respectively.[8,9] Thus, the artificial WS_2/MoS_2 heterostructure has the strongest dielectric screening effect compared with the monolayer counterparts. Consequently, the CP energies redshift in the heterostructure film compared with that of the 1L-WS_2 and 1L-MoS_2 film. This is a consequence of

Published on 03 November 2020. Downloaded by Changchun Institute of Optics, Fine Mechanics and Physics, CAS on 4/2/2021 4:48:27 AM.

Table 1 CP energies (E_{th}) for monolayer and heterostructure samples. M_0, M_1, and the non-defined type of Van Hove singularities are indicated in purple, orange, and blue, respectively

CP energies/eV	MoS_2	WS_2	WS_2/MoS_2
A	1.88 ± 0.016	2.02 ± 0.015	1.86 ± 0.044
B	2.00 ± 0.111	2.40 ± 0.024	1.89 ± 0.018
C	2.87 ± 0.014	2.82 ± 0.207	2.03 ± 0.005
D	3.27 ± 0.178	3.09 ± 0.015	2.28 ± 1.332
E	4.00 ± 0.356	3.20 ± 0.097	2.80 ± 0.043
F	4.56 ± 0.349	3.70 ± 0.330	3.10 ± 0.803
G	5.00 ± 0.564	4.36 ± 0.075	4.26 ± 0.737
H	5.96 ± 0.553	4.50 ± 0.458	4.50 ± 1.167
I	—	5.75 ± 0.764	4.62 ± 1.100
J	—	—	5.52 ± 0.243

the weakened Coulomb interactions, which decreases the electronic quasi-particle (QP) band gap (*i.e.* smaller CP energies).

Most recently, the specific transition positions of these peaks in the BZ of 1L-WS_2 and 1L-MoS_2 films have been studied in detail in the literature.[3,21,25] As expected, our CP energies of 1L-TMDs are in excellent agreement with that of these previous studies. Thus, here we focus on the investigation of specific transition positions of CPs in the WS_2/MoS_2 heterostructure and the types of *Van Hove singularities* of all these samples.

CPs or singularities of the joint density of states (*i.e.*, *Van Hove singularities*) are expected to occur under two conditions: first, the slopes of the valence and conduction bands are horizontal; second, the slopes of the two bands are parallel. Nevertheless, the CPs behave differently depending on their type of *Van Hove singularities*.[34] Most notably, 2D materials only have M_0, M_1, and M_2 types of *Van Hove singularities*.[34–36] As reported in previous studies, A_M, A_W, B_H and C_H CPs are the transitions at the K point in the BZ of 1L-MoS_2, 1L-WS_2 and the WS_2/MoS_2 heterostructure, respectively.[17,37,38] As expected, the exact transition energies of the A_M, A_W, B_H and C_H CPs are consistent with the PL peaks in Fig. S3.† Remarkably, in the case of the WS_2/MoS_2 heterostructure, B_H CP is aligned to the transition between two Mo orbits, in analogy with A_M CP, whereas the C_H CP is attributed to the transition between two W orbits, in analogy with the A_W CP.[9,17] These transitions usually occur along the six equivalent [111] directions (K point) of the BZ, referred to as the E_1 *transition* in 2D materials. In addition, ε_2 typically rises to an asymmetric peak at the corresponding energy positions, as shown in Fig. 2a. Furthermore, the groups of symmetry of 1L-MoS_2, 1L-WS_2, and the WS_2/MoS_2 heterostructure lack inversion symmetry, and as a result the valence bands present a sizable spin–orbit interaction. This will lead to a split-off valence band labelled the $E_1 + \Delta_1$ *transition*, corresponding to B_M, B_W, D_H and E_H CPs of 1L-MoS_2, 1L-WS_2 and WS_2/MoS_2 heterostructure samples, respectively.[36] Similar to the case of B_H and C_H CPs, D_H and E_H are assigned to transitions between two Mo and W orbits, in analogy with B_M and B_W CP, respectively. Meanwhile, A_H CP is attributed to an interlayer transition from W to Mo orbits locating at the K point in the BZ of the heterostructure,[9] where the VBM locates at the WS_2 layer and CBM locates at the MoS_2 layer.[9,17] More importantly, the band structures of the aforementioned eight CPs (A–B_M, A–B_W, and A–D_H) suggested that these transitions are often modelled by a 2D M_0 type CP, indexed purple in Fig. 2a and Table 1. The effect that many more CPs occur at K points in the BZ of heterostructure compared with the number of CPs in 1L-TMDs can be attributed to the increased dielectric screening in the WS_2/MoS_2 heterostructure, and the orbital overlap leads to nontrivial changes in the higher conduction and deeper valence regions, *i.e.* hybridization energy gaps.[39]

Furthermore, as shown in Fig. 2a (orange area, indexed orange in Table 1 as well), the $\varepsilon_2(E)$ of the three samples reached a strong absolute maximum known as the E_2 peak. The E_2 peak contains contributions from transitions occurring over a large region in the BZ,[36] thus explaining the strong intensities of these peaks. Some of these transitions are associated with M_1 *critical points*.[34] As for WS_2/MoS_2 heterostructure films, referring to the previous calculation results of their band structure,[17] the E_2 peak results from the combined contribution of the transitions in a wide area. It contains the area between the Γ points and Λ point (midpoint along Γ–K direc-

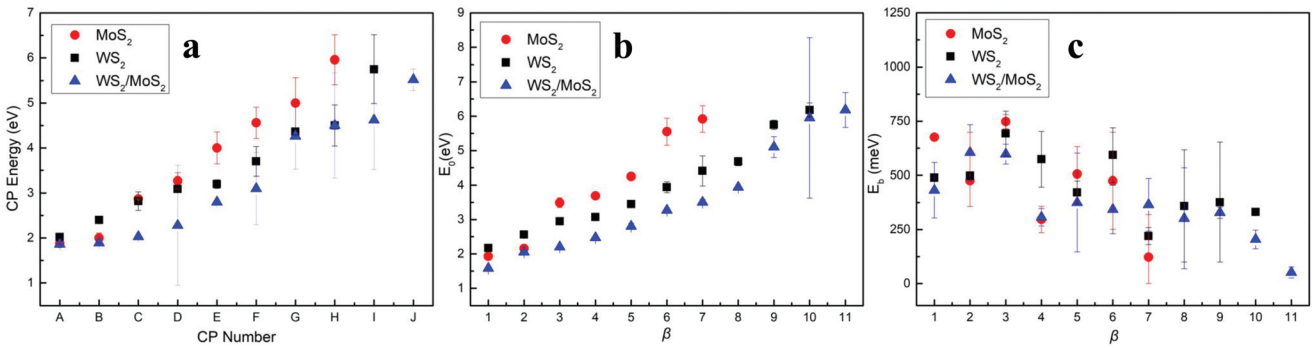

Fig. 3 (a) CP energies. Red circles, black squares, and blue triangles represent the CP energies of 1L-MoS_2, 1L-WS_2 and the WS_2/MoS_2 heterostructure, respectively. (b and c) Excitonic transition energies E_0 and binding energies E_b obtained by fitting the absorption coefficient spectrum ($\alpha(E)$) of the monolayer and heterostructure samples.

This journal is © The Royal Society of Chemistry 2020

Published on 03 November 2020. Downloaded by Changchun Institute of Optics, Fine Mechanics and Physics, CAS on 4/2/2021 4:48:27 AM.

tion), and the area from the midpoint along the M–Γ direction to the Γ points in the BZ, wherever there exist parallel valence bands and conduction bands. This distribution can be confirmed through the well agreement of the CP energies we obtained and the required transition energies from valence bands to the conduction band in the BZ. There are several weaker structures labelled as E′$_0$ and E′$_1$ *transitions*, *i.e. saddle critical points*, superimposed on the above features. These CPs involve transitions between the valence bands to the higher conduction bands at the BZ centre (Γ point) and along the [111] directions, respectively.[36] Moreover, no M_2 critical points have been identified in the optical spectra, as a result of the strong suppression of the singularity in the optical transition strength. Moreover, in practice, the higher energy transitions are usually found to contain contributions from several different types of CPs.[36] Thus, it is hard to define their singularities. The non-defined type CPs are indexed blue in Fig. 2a and Table 1.

According to the exacted transition energies of CPs in Table 1, the spin–orbit splitting Δ_1 of 1L-WS_2 and 1L-MoS_2 can be calculated by eqn (6):[36]

$$\begin{cases} \Delta_{1M} = B_M - A_M = 120\ \text{meV} \\ \Delta_{1W} = B_W - A_W = 380\ \text{meV} \end{cases} \quad (6)$$

where, Δ_{1M} and Δ_{1W} represent the spin–orbit splitting of 1L-MoS_2 and 1L-WS_2, respectively. The Δ_1 values of 1L-TMDs obtained from eqn (6) agree well with that of previous first-principles calculations.[37,38]

3.4. Exciton properties

The optical properties of 2D materials are not only strongly correlated to their quasiparticle band structures but also significantly influenced by the large excitonic effects.[40] In particular, very recent first-principle calculation studies revealed that the different natures of excitons in monolayer and heterostructure films are mainly caused by the dielectric screening,[11] while the quantum confinement effect will not significantly influence the vertical dielectric screening of van der Waals semiconductors with few layers.[8] Thus, investigation of the dielectric screening has become a very exciting research field for exploring excitonic properties of heterostructures.

The absorption coefficient spectra ($\alpha(E)$) of the samples are depicted in ESI as Fig. S6b.† Nevertheless, because of the strong excitonic effects in low-dimensional thin films, it is not accurate to simply extract the gap energy using the linear extrapolation of absorption coefficients (LEA) method.[3] Fortunately, the discrete states of the exciton observed in 1L-TMDs and heterostructure thin films can be modelled using a broaden Lorentzian line shape:[20,33,41]

$$\alpha(E) = \mathrm{Im}\left[\sum_{\beta=A,B,C,\ldots}\left(\sum_{n=1}^{\infty}\frac{A_{0\beta}}{n^3}\frac{1}{E_{0\beta}-\frac{R_\beta}{n^2}-E-i\Gamma_{\mathrm{ex},n}}\right)\right] \quad (7)$$

where β is the index number of valence band; n is the index number of the excitonic excited states; $\Gamma_{\mathrm{ex},n}$ is the broadening parameter of the nth excited states; and $E_{0\beta}$ is the transition energy. Additionally, different from the CP transition energies (E_{th}), owing to the weak attraction between electron and hole pair building an exciton, $E_{0\beta}$ is numerically less than the corresponding interband transition energies; $A_{0\beta}$ is an adjustable fitting parameter; and R_β is the Rydberg constant for the exciton defined as:[34–36]

$$R_\beta = \frac{\mu e^4}{2(4\pi\varepsilon_0\hbar)^2\varepsilon_r{}^2} = \left(\frac{\mu}{m_0\varepsilon_r{}^2}\right)\times 13.6\ \text{eV} \quad (8)$$

where the 13.6 eV is the ionization energy for the hydrogen atom, μ denotes the reduced effective mass $\mu^{-1} = m_e^{*-1} + m_h^{*-1}$, and m_0 is the effective mass of electron. In the case of 2D materials, it is well known that the exciton binding energy is enhanced due to spatial confinement and reduced environment dielectric screening. Thus, the exciton binding energy of 2D materials is defined as eqn (9):[42]

$$E_b(n) = -\frac{1}{(n-1/2)^2}R_\beta \quad (9)$$

As for the excitonic ground state (n = 1), the excitonic binding energy $E_b^{2D}(1)$ = $4R_\beta$. Due to the restriction of the momentum conservation law and negligible photon wave number in comparison to the first BZ, the spectrum of excitons is a series of discrete levels. Where necessary, we have assumed that the kinetic energy of the center of mass of excitons is zero, and so the spectrum of excitons is given as:[35]

$$E_0(n) = E_g - E_b(n) \quad (10)$$

where E_g is the QP band gap, which is equal to the CP energy at *Van Hove singularities*. Using the aforementioned broadened Lorentzian line shape, we obtained the excitonic transition energies and binding energies of 1L-MoS_2, 1L-WS_2, and the WS_2/MoS_2 heterostructure. Owing to the limitations of the model (eqn (7)), only the properties of the excitonic ground state can be fitted. Our best-fitting curves and the measurement curves are shown in ESI as Fig. S8.† The list of fitting parameters is given as Table S2† in the ESI.†

Fig. 3b and c compare the transition energies (E_0) and the binding energies (E_b) of the excitons in 1L-MoS_2, 1L-WS_2, and the WS_2/MoS_2 heterostructure. Consequently, compared with conventional semiconductor materials, the large exciton binding energies of 1L-WS_2, 1L-MoS_2 and the WS_2/MoS_2 heterostructure have been experimentally proven, which is the key factor rendering them stable even at room temperature. It is apparent that the interlayer exciton (transition energy E_0: 1.58 ± 0.050 eV) in the heterostructure presents a lower excitonic binding energy (431.39 ± 127.818 meV) than those of the adjacent intralayer excitons (Fig. 3c), which can be attributed to the special separation of the electrons and holes in the case of interlayer ones. The fitted transition energy of the interlayer exciton from $\alpha(E)$ is consistent with its PL peak position (1.60 eV), and the small oscillator strength of the interlayer exciton peak in the ($\alpha(E)$) (Fig. S8c†) is also the result of the spatially separated charge carriers.[17] Moreover, from a practical point of

Published on 03 November 2020. Downloaded by Changchun Institute of Optics, Fine Mechanics and Physics, CAS on 4/2/2021 4:48:27 AM.

view, this longer lifetime but lower binding energy exciton can be used to optimize the performance of next-generation optoelectronic and photonic devices based on excitons.

In addition, the internal Coulomb interaction, which determines the properties of excitons in 2D materials, is strongly coupled with the surrounding dielectric medium. This is referred to a dielectric screening effect.[42] Stacking 1L-MoS_2 (ε_{MoS2} = 6.3) on 1L-WS_2 (ε_{WS2} = 6.0) reassembles the artificial WS_2/MoS_2 heterostructure with a larger effective dielectric constant (ε_{WS_2/MoS_2} = 6.5). Fig. 3c shows that, as expected, the increased dielectric screening in the case of heterostructures reduces the excitonic binding energy compared with those of monolayer TMDs excitons, which results from the larger screened electron–hole interaction in the WS_2/MoS_2 heterostructure film, although there are two abnormal data points (β = 2 and 7) that may be caused by calculation errors. Furthermore, as shown in Fig. 3b, the increased dielectric screening in the WS_2/MoS_2 heterostructure film also redshifts the transition energies of excitons compared to the 1L-TMD ones. Meanwhile, as revealed by the aforementioned CP section, the QP is decreased by the high surrounding dielectric constant, as well as the excitonic binding energies. In these circumstances, the excitonic transition energies of 1L-TMDs are higher than those of the WS_2/MoS_2 heterostructure, indicating that the regulatory effect of dielectric screening is not large enough to change the relative positions of the exciton energy levels, which depends on the QP band alignment of 1L-MoS_2, 1L-WS_2, and the WS_2/MoS_2 heterostructure. Notably, the dielectric screening of the substrate will influence not only the CP positions but also the exciton transition energies and binding energies of the upper film. Thus, based on the control variable method, all the measurements in this study have been carried out on sapphire substrates. The peak shift or energy difference between our results and other studies that also used sapphire substrates can be attributed to different synthesis methods, transition procedures, annealing temperatures, annealing time or other factors, because charge doping, strain or inhomogeneity can cause changes in the linewidths and position of the narrow exciton peaks in the spectral response.[43] Our results may provide a route to control optical and electronic properties of 1L-TMDs at room temperature, which opens up possibilities for various optoelectronic applications, such as photoelectric detectors with adjustable response wavelengths.

4. Conclusion

In summary, we employed SE to investigate the excitonic and critical points properties of the WS_2/MoS_2 heterostructure. As a result of the orbital hybridization in deeper valence and higher conduction band regions of the WS_2/MoS_2 heterostructure, more CPs were found. Also, the increasing dielectric screening in the WS_2/MoS_2 heterostructure weakens the Coulomb interactions, which results in the redshift of the CP energies, excitonic transition energies and binding energies in the heterostructure compared with those of 1L-TMDs films. The decrease in CP energies indicates the reduced QP band gap. Specifically, the environment dielectric has more effect on the QP band than the excitonic binding energy. Moreover, owing to the charge carrier spatial separation, the dipole oscillator strength of the interlayer exciton is much smaller than that of the intralayer exciton. Thus, the interlayer excitonic peak in the absorption spectra is practically invisible, as predicted by Engin Torun *et al.* in a very recent first-principles investigation.[17] The transition energy (E_0: 1.58 ± 0.050 eV) and binding energy (E_b: 431.39 ± 127.818 meV) of the interlayer exciton are obtained by fitting the absorption coefficient spectra ($\alpha(E)$) with a broaden Lorentzian line shape. In addition, a larger optical conductivity was obtained in the WS_2/MoS_2 heterostructure than with that of 1L-WS_2 and 1L-MoS_2. Our findings prove that stacked vertical heterostructures have emerged as a powerful strategy for tuning the effective dielectric screening of 1L-TMD films, which is very important for their applications in nanoelectronic and optoelectronic devices.

Conflicts of interest

There is no conflict of interest to declare.

Acknowledgements

The work was financially supported by the National Natural Science Foundation of China (Grant 11674062, 61775042, 61774040), International S&T Cooperation Program of China (Grant 2016YFE0110700), and the Fudan University – CIOMP Joint Fund (FC2019-006).

References

1 L. Liang and V. Meunier, *Nanoscale*, 2014, **6**, 5394.
2 A. Molina-Sánchez, D. Sangalli, K. Hummer, A. Marini and L. Wirtz, *Phys. Rev. B: Condens. Matter Mater. Phys.*, 2013, **88**, 2358–2367.
3 J. W. Park, H. S. So, S. Kim, S. H. Choi, H. Lee, J. Lee, C. Lee and Y. Kim, *J. Appl. Phys.*, 2014, **116**, 183509.
4 H. P. Komsa and A. V. Krasheninnikov, *Phys. Rev. B: Condens. Matter Mater. Phys.*, 2012, **86**, 233–243.
5 A. K. Geim and I. V. Grigorieva, *Nature*, 2013, **499**, 419–425.
6 A. Pant, Z. Mutlu, D. Wickramaratne, H. Cai, R. K. Lake, C. Ozkan and S. Tongay, *Nanoscale*, 2016, **8**, 3870–3887.
7 W. Xia, L. Dai, P. Yu, X. Tong, W. Song, G. Zhang and Z. Wang, *Nanoscale*, 2017, **9**, 4324–4365.
8 J. Koo, S. Gao, H. Lee and L. Yang, *Nanoscale*, 2017, **9**, 14540–14547.
9 S. Gao, L. Yang and C. D. Spataru, *Nano Lett.*, 2017, **17**, 7809–7813.
10 C. R. P. Inbaraj, R. J. Mathew, R. K. Ulaganathan, R. Sankar, M. Kataria, H. Y. Lin, H. Y. Cheng, K. H. Lin,

 This journal is © The Royal Society of Chemistry 2020

Published on 03 November 2020. Downloaded by Changchun Institute of Optics, Fine Mechanics and Physics, CAS on 4/2/2021 4:48:27 AM.

H. I. Lin, Y. M. Liao, F. C. Chou, Y. T. Chen, C. H. Lee and Y. F. Chen, *ACS Appl. Mater. Interfaces*, 2020, **12**, 26213–26221.
11 S. Latini, T. Olsen and K. S. Thygesen, *Phys. Rev. B: Condens. Matter Mater. Phys.*, 2015, **92**, 245123.
12 K. Andersen, S. Latini and K. S. Thygesen, *Nano Lett.*, 2015, **15**, 4616–4621.
13 A. Raja, A. Chaves, J. Yu, G. Arefe, H. M. Hill, A. F. Rigosi, T. C. Berkelbach, P. Nagler, C. Schüller, T. Korn, C. Nuckolls, J. Hone, L. E. Brus, T. F. Heinz, D. R. Reichman and A. Chernikov, *Nat. Commun.*, 2017, **8**, 15251.
14 J. Shim, D. H. Kang, Y. Kim, H. Kum, W. Kong, S. H. Bae, I. Almansouri, K. Lee, J. H. Park and J. Kim, *Carbon*, 2018, **133**, 78–89.
15 T. Deilmann and K. S. Thygesen, *Nano Lett.*, 2018, **18**, 1460–1465.
16 X. Hong, J. Kim, S. F. Shi, Y. Zhang, C. Jin, Y. Sun, S. Tongay, J. Wu, Y. Zhang and F. Wang, *Nat. Nanotechnol.*, 2014, **9**, 682–686.
17 E. Torun, H. P. C. Miranda, A. M. Sánchez and L. Wirtz, *Phys. Rev. B*, 2018, **97**, 245427.
18 W. Hu and J. Yang, *J. Mater. Chem. C*, 2017, **5**, 12289–12297.
19 L. Waldecker, A. Raja, M. Rosner, C. Steinke, A. Bostwick, R. J. Koch, C. Jozwiak, T. Taniguchi, K. Watanabe, E. Rotenberg, T. O. Wehling and T. F. Heinz, *Phys. Rev. Lett.*, 2019, **123**, 206403.
20 H. L. Liu, C. C. Shen, S. H. Su, C. L. Hsu, M. Y. Li and L. J. Li, *Appl. Phys. Lett.*, 2014, **105**, 201905.
21 W. Li, A. G. Birdwell, M. Amani, R. A. Burke, X. Ling, Y. H. Lee, X. Liang, L. Peng, C. A. Richter and J. Kong, *Phys. Rev. B: Condens. Matter Mater. Phys.*, 2014, **90**, 195434.
22 D. H. Li, H. Zheng, Z. Y. Wang, R. J. Zhang, H. Zhang, Y. X. Zheng, S. Y. Wang, D. W. Zhang and L. Y. Chen, *Phys. Chem. Chem. Phys.*, 2017, **19**, 12022–12031.
23 M. R. Laskar, L. Ma, S. Kannappan, P. S. Park, S. Krishnamoorthy, D. N. Nath, W. Lu, Y. Wu and S. Rajan, *Appl. Phys. Lett.*, 2013, **102**, 252108.
24 Y. Zhang, Y. Zhang, Q. Ji, J. Ju, H. Yuan, J. Shi, T. Gao, D. Ma, M. Liu, Y. Chen, X. Song, H. Y. Hwang, Y. Cui and Z. Liu, *ACS Nano*, 2013, **7**, 8963–8971.
25 H. G. Park, T. J. Kim, H. S. Kim, C. H. Yoo, N. S. Barange, V. L. Le, H. U. Kim, V. Senthilkumar, C. T. Le, Y. S. Kim, M. J. Seong and Y. D. Kim, *Appl. Spectrosc. Rev.*, 2016, **51**, 621–635.
26 F. Ceballos, M. Z. Bellus, H. Y. Chiu and H. Zhao, *Nanoscale*, 2015, **7**, 17523.
27 C. Gong, H. Zhang, W. Wang, L. Colombo, R. M. Wallace and K. Cho, *Appl. Phys. Lett.*, 2013, **103**, 053513.
28 H. Li, Q. Zjamg, C. C. R. Yap, B. K. Tay, T. H. T. Edwin, A. Olivier and D. Baillargeat, *Adv. Funct. Mater.*, 2012, **22**, 1385–1390.
29 N. Peimyoo, J. Shang, W. Yang, Y. Wang, C. Cong and T. Yu, *Nano Res.*, 2015, **8**, 1210–1221.
30 N. Peimyoo, W. Yang, J. Shang, X. Shen, Y. Wang and T. Yu, *ACS Nano*, 2014, **8**, 11320–11329.
31 J. P. Xu, R. J. Zhang, Y. Zhang, Z. Y. Wang, L. Chen, Q. H. Huang, H. L. Lu, S. Y. Wang, Y. X. Zheng and L. Y. Chen, *Phys. Chem. Chem. Phys.*, 2016, **18**, 3316–3321.
32 K. F. Mak, C. Lee, J. Hone, J. Shan and T. F. Heinz, *Phys. Rev. Lett.*, 2010, **105**, 474–479.
33 X. Zhu, D. Li, R. Zhang, H. Zhang, C. Cong, M. Zhu, Y. Shi, Y. Wu, S. Wang, Y. Zheng and L. Chen, *Appl. Surf. Sci.*, 2020, **519**, 146262.
34 *Basic Semiconductor Physics*, ed. C. Hamaguchi, Springer, Heidelberg, 2010.
35 *The Physics of Semiconductors*, ed. M. Grundmann, Springer, Berlin Heidelberg, 2006.
36 *Fundamentals of Semiconductors: Physics and Materials Properties*, ed. P. Y. Yu and M. Cardona, Springer, Heidelberg, 2010.
37 J. E. Padilha, H. Peelaers, A. Janotti and C. G. V. Walle, *Phys. Rev. B: Condens. Matter Mater. Phys.*, 2014, **90**, 205420.
38 C. Cong, J. Shang, Y. Wang and T. Yu, *Adv. Opt. Mater.*, 2018, **6**, 1700767.
39 N. B. Le, T. D. Huan and L. M. Woods, *ACS Appl. Mater. Interfaces*, 2016, **8**, 6286–6292.
40 J. Shang, X. Shen, C. Cong, N. Peimyoo, B. Cao, M. Eginligil and T. Yu, *ACS Nano*, 2015, **9**, 647–655.
41 J. F. Muth, R. M. Kolbas, A. K. Sharma, S. Oktyabrsky and J. Narayan, *J. Appl. Phys.*, 1999, **85**, 7884–7887.
42 M. D. Tran, J. H. Kim and Y. H. Lee, *Curr. Appl. Phys.*, 2016, **16**, 1159–1174.
43 Y. Li, A. Chernikov, X. Zhang, A. Rigosi, H. M. Hill, A. M. Zande, D. A. Chenet, E. M. Shih, J. Hone and T. F. Heinz, *Phys. Rev. B: Condens. Matter Mater. Phys.*, 2014, **90**, 205422.